High-performance sodium–organic battery by realizing four-sodium storage in disodium rhodizonate

Minah Lee [1], Jihyun Hong[2,3], Jeffrey Lopez [1], Yongming Sun[2], Dawei Feng[1], Kipil Lim[2,3], William C. Chueh[2], Michael F. Toney [3], Yi Cui[2]* and Zhenan Bao[1]*

Sodium-ion batteries (SIBs) for grid-scale applications need active materials that combine a high energy density with sustainability. Given the high theoretical specific capacity 501 mAh g^{-1}, and Earth abundance of disodium rhodizonate ($Na_2C_6O_6$), it is one of the most promising cathodes for SIBs. However, substantially lower reversible capacities have been obtained compared with the theoretical value and the understanding of this discrepancy has been limited. Here, we reveal that irreversible phase transformation of $Na_2C_6O_6$ during cycling is the origin of the deteriorating redox activity of $Na_2C_6O_6$. The active-particle size and electrolyte conditions were identified as key factors to decrease the activation barrier of the phase transformation during desodiation. On the basis of this understanding, we achieved four-sodium storage in a $Na_2C_6O_6$ electrode with a reversible capacity of 484 mAh g^{-1}, an energy density of 726 Wh kg$^{-1}_{cathode}$, an energy efficiency above 87% and a good cycle retention.

The rise of renewable solar and wind power is demanding sustainable storage technologies using components that are inexpensive, Earth-abundant and environmental friendly[1]. This has prompted research on the development of sodium-ion batteries (SIBs) because of sodium's low cost and its inexhaustible resources[2]. There have been exciting advances in the performance of SIBs utilizing layered transition-metal oxides and polyanions, which suggest that the sodium compounds can be promising compared with their lithium analogues[3]. The layered metal oxides offer high energy densities but are limited by cycling stability and air sensitivity, whereas polyanions show rather stable cycle life but only deliver a moderate energy density. Thus, further research is required to find better sodium host materials[4]. In addition, material sustainability is also a critical factor when considering the total economic and environmental benefits for grid-scale energy storage applications[5].

Organic compounds that can be obtained from natural biomass with minimum energy consumption are an attractive low-cost and sustainable choice for battery electrode materials, provided a high energy density and long cycling stability can be obtained[6–8]. Rhodizonate ionic crystals that are readily prepared from a natural compound myo-inositol from plants have been proposed as promising active compounds for rechargeable batteries owing to their exceptional theoretical energy density[9]. Dilithium rhodizonate ($Li_2C_6O_6$) was first reported in 2008 by Tarascon and colleagues, who reported that it exhibited a theoretical capacity of 560 mAh g^{-1} based on a four-electron redox chemistry in lithium-ion batteries[10]. However, $Li_2C_6O_6$ showed poor cycle stability due to dissolution and exfoliation of the material, which limits its practical application[11,12]. Later work turned to disodium rhodizonate ($Na_2C_6O_6$), and demonstrated excellent cycle stability in SIB[13]. Although it seemed intuitive to expect a similar four-electron redox reaction in $Na_2C_6O_6$, previous studies have experienced challenges in repeatedly utilizing

four electrons[14,15]. Rather, there was a substantial capacity loss after the first cycle, and the following reversible capacity was much lower than its theoretical capacity of 501 mAh g^{-1}. Despite its crucial importance, the origin of this discrepancy remains unknown.

Here, we reveal the origin of the limited electrochemical performance of $Na_2C_6O_6$ and provide an effective path to achieve reversible four-sodium storage. We identified that a reversible phase transformation, which is kinetically limited during desodiation, is a requirement for the four-electron redox reaction of $Na_2C_6O_6$. The reversible phase transformation of $Na_2C_6O_6$ accompanied by spontaneous nanostructuring of the active particles is achieved by decreasing the size of the active particles and selecting proper electrolytes, which provides a mechanism to realize efficient four-sodium storage with a specific capacity of 484 mAh g^{-1}. Our work highlights the importance of understanding redox mechanisms for effective utilization of redox compounds, which opens up new opportunities to build a high-performance and sustainable energy storage system.

Crystal structure and morphology of $Na_2C_6O_6$
$Na_2C_6O_6$ has alternating layers of hexagonally packed Na$^+$ cations and rhodizonate dianions ($C_6O_6^{2-}$) where the cations lie $a/4$ above the anions (space group $Fddd$)[16], as shown in Fig. 1a. Each Na$^+$ ion coordinates with eight total oxygen atoms from four different rhodizonate dianions, thereby connecting adjacent C_6O_6 layers in the structure. This sodium–oxygen ionic bond is highly stable in most organic solvents and so prevents dissolution of the $Na_2C_6O_6$ into conventional electrolytes based on carbonate and ether solvents (Supplementary Fig. 1a). The carbonyl groups are known to act as redox active sites in oxocarbon salts[10,17]. Thus, $Na_2C_6O_6$ is expected to store four Na ions per formula unit with a theoretical specific capacity of 501 mAh g^{-1}, which has not been demonstrated experimentally so far.

[1]Department of Chemical Engineering, Stanford University, Stanford, CA 94305, USA. [2]Department of Materials Science and Engineering, Stanford University, Stanford, CA 94305, USA. [3]Stanford Synchrotron Radiation Lightsource, SLAC National Accelerator Laboratory, Menlo Park, CA 94025, USA.
*e-mail: yicui@stanford.edu; zbao@stanford.edu
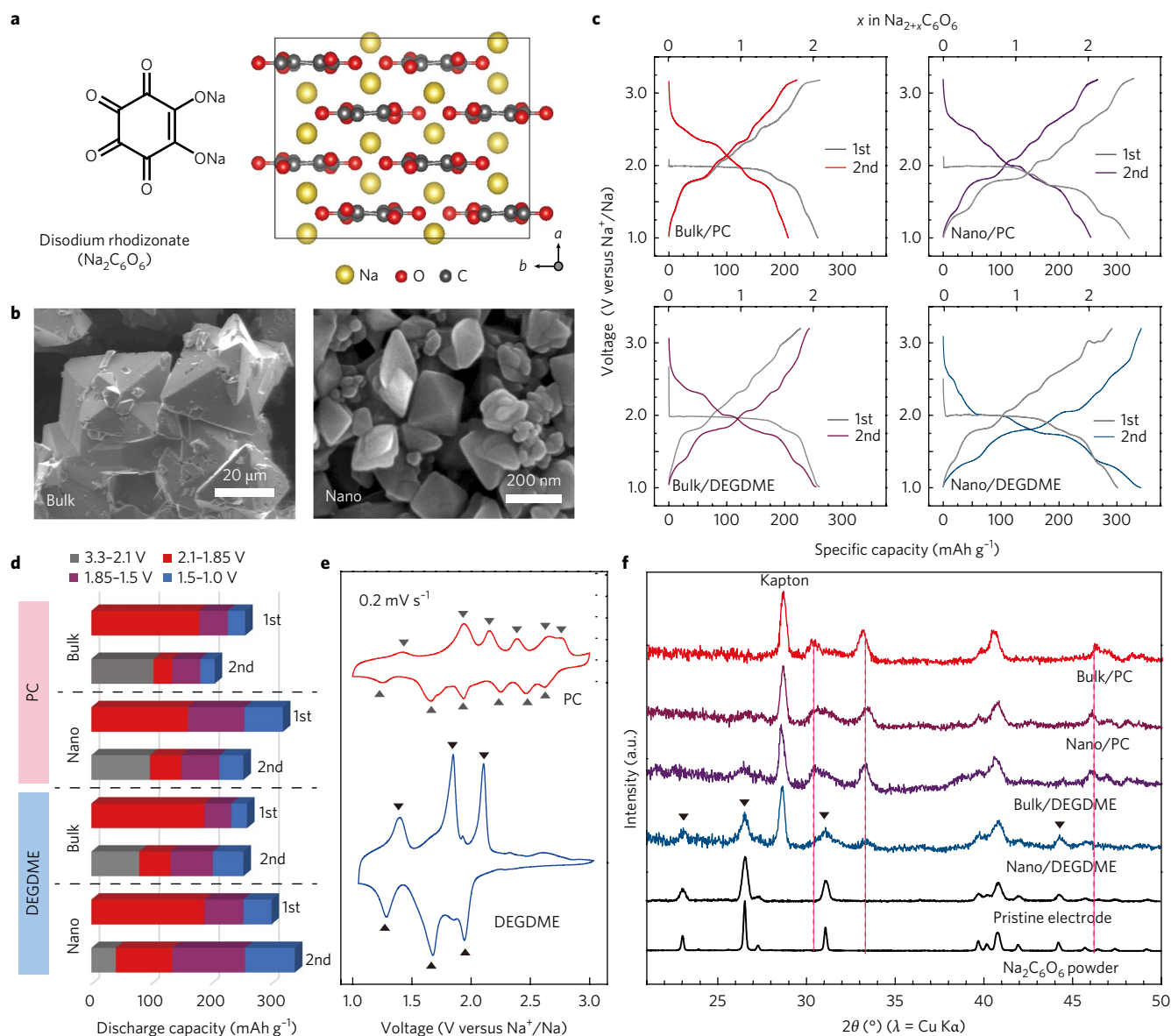
Fig. 1 | Structure of Na$_2$C$_6$O$_6$ and its electrochemical behaviour in Na cells under different conditions showing inconsistent phase transition. a, Chemical and crystal structures of Na$_2$C$_6$O$_6$. **b**, SEM images of bulk and nanoparticles used to prepare Na$_2$C$_6$O$_6$ electrodes. **c**, First and second discharge/charge cycles of Na$_2$C$_6$O$_6$ electrodes with different particle sizes and electrolyte conditions. **d**, Stacked bar chart of discharge capacities for different conditions. The separate capacities from different plateau regions were assigned to different bars with distinctive colours. **e**, Typical cyclic voltammograms of nanoparticle electrodes in PC and DEGDME electrolytes after the first cycle at 0.2 mV s^{-1}. **f**, XRD patterns of Na$_2$C$_6$O$_6$ electrodes after the first discharge/charge cycle compared with that of the pristine powder and electrode.

Electrochemistry of Na$_2$C$_6$O$_6$ in Na-ion cells

During our initial test of Na cells according to literature-reported conditions using Na$_2$C$_6$O$_6$ of several tens of micrometres (Bulk, Fig. 1b) as the cathode, a metallic sodium anode, and a propylene carbonate (PC) electrolyte in a potential window of 1.0 to 3.2 V, we also observed a limited capacity of less than 260 mAh g^{-1} (2.1 Na) for the first discharge/charge cycle and a capacity of 210 mAh g^{-1} (1.7 Na) for the following cycles (Fig. 1c, Bulk/PC), consistent with the results in previous studies using carbonate-based electrolytes[13–15]. Nevertheless, we highlight two important features in this voltage profile: the large discrepancy in capacities between the first and subsequent cycles, and the difference between the first discharge profile with a pronounced plateau at 2.0 V versus Na$^+$/Na, and the following charge/discharge profiles with more sloped and multiple plateaus. Note that the morphology change of bulk

particles during cycling was not significant enough to induce such hysteresis (Supplementary Fig. 2 and Supplementary Note 1). In the following experiment, we tested Na$_2$C$_6$O$_6$ particles of a few hundred nanometres (Nano) to improve the reaction kinetics (Fig. 1b and Supplementary Fig. 3), and still found similar profile evolution and deteriorating redox activity (Fig. 1c, Nano/PC). Therefore, we ascribe this change to irreversible redox reaction, in other words, different reaction pathways between the initial and subsequent sodiation processes.

To our surprise, the Na$_2$C$_6$O$_6$ electrode in diethylene glycol dimethyl ether (DEGDME) electrolyte showed distinctive voltage profiles when compared with the profiles in PC electrolyte (Fig. 1c). First, there was no capacity loss after the first cycle; for the bulk particle electrode (Bulk/DEGDME), the capacity was almost identical for the first and following cycles, and for the nanoparticle electrode

(Nano/DEGDME), the capacity was even increased in the second cycle. Moreover, in Nano/DEGDME, the plateau at 2.0 V in the initial discharge was clearly maintained in the second discharge and the short sloping region below 1.9 V further evolved into well-defined plateaus, resulting in a reversible specific capacity of 350 mAh g^{-1}. When testing Na$_2$C$_6$O$_6$ particles on the order of a few micrometres (Micro/DEGDME), the performance was in between that of Bulk/DEGDME and Nano/DEGDME (Supplementary Fig. 4), which further validates our finding on the size effect that determines voltage profile evolution and reversible capacity in DEGDME electrolyte.

For better comparison, Fig. 1d shows a stacked bar chart illustrating separate discharge capacities in different voltage ranges from the above conditions. When comparing the separate discharge capacities in the second cycle from the plateau region of 2.10–1.85 V, which is dominant in the first cycle, it is clear that Nano/DEGDME shows the most capacity in the original plateau regions. In contrast, Bulk/PC exhibits the least capacity in this region, which ends up with the smallest overall capacity among the conditions in the second cycle. The cyclic voltammograms for Nano/PC and Nano/DEGDME (Fig. 1e) further demonstrate the clear distinction in the redox peaks between the electrolytes. Six pairs of redox peaks were identified in PC, whereas only three dominant peaks were observed in DEGDME, indicating a significant difference in the reaction paths between the electrolytes. Note that both PC and DEGDME electrolytes exhibit good wettability on Na$_2$C$_6$O$_6$ electrode surfaces (Supplementary Fig. 1b).

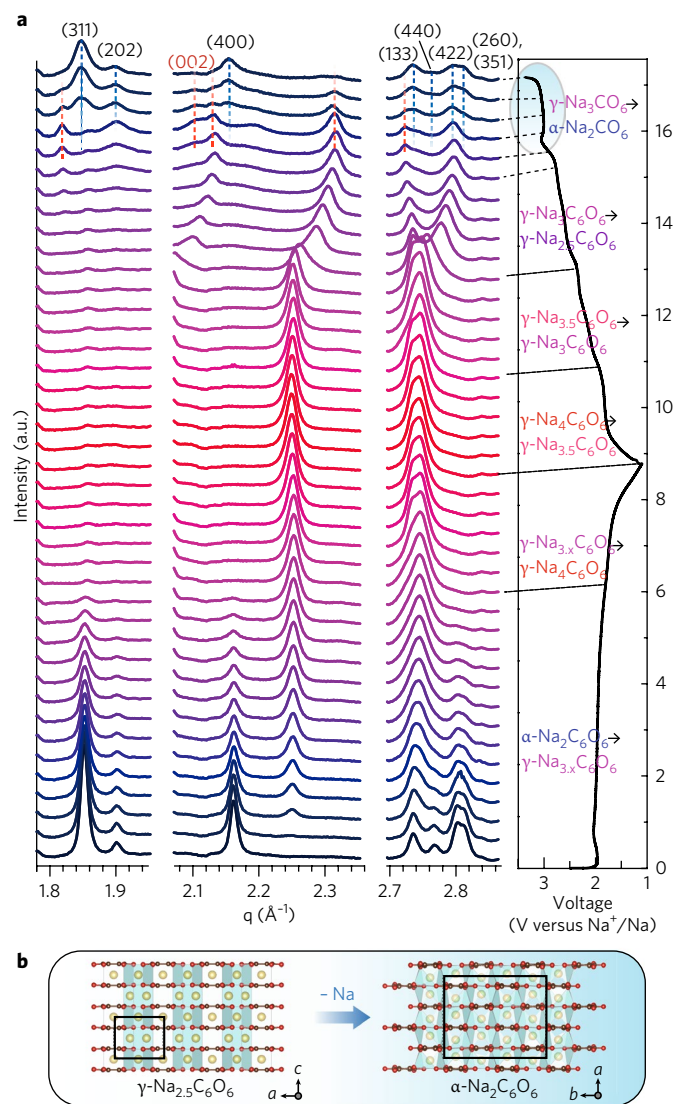## Phase transformation of Na$_2$C$_6$O$_6$ during the first cycle

To reveal the origin of voltage profile evolution between cycles and inconsistent electrochemical behaviours in different conditions, we examined whether the phase change of Na$_2$C$_6$O$_6$ was reversible after cycling. We collected X-ray diffraction (XRD) patterns of the electrodes retrieved from cycled Na cells in each condition at the end of the first discharge/charge cycle (Fig. 1f). The pristine electrode exhibits diffraction peaks identical to that of Na$_2$C$_6$O$_6$ powder at 23.0°, 26.5° and 31.1° corresponding to the (131), (311) and (400) planes, respectively. We found that the diffraction patterns of the cycled electrodes did not completely match with its original phase. Rather, new peaks in the cycled samples were identified (as indicated with red dashed lines in Figure 1f), which show different intensities depending on the cycling conditions. The formation of the new phase during sodium insertion in Na$_2$C$_6$O$_6$ was theoretically studied previously[18,19]. Following sodiation, the original C$_6$O$_6$ stacking (termed the α-phase), where the C$_6$O$_6$ layers are laterally displaced, is not energetically favourable anymore due to the additional electrons filling up unoccupied e_{1g} orbitals. The most stable structure for Na$_{2+x}$C$_6$O$_6$ calculated using density functional theory (DFT) is a new layered structure in which the C$_6$O$_6$ molecules lie directly over each other, termed the γ-phase (Supplementary Fig. 5a,b). When comparing the predicted XRD pattern of Na$_{2+x}$C$_6$O$_6$ from DFT calculations (Supplementary Figs. 5c and 6c) with our ex situ XRD results, the new peaks in the cycled electrodes can be attributed to the residual γ-phase containing more than two sodium atoms per formula. As the original α-phase is not fully recovered after the first cycle in most conditions, it is clear that the following sodiation would start in this new γ-phase, resulting in a reaction path different from the initial cycle. This can explain the inconsistent voltage profiles between the first and the following cycles.

We fitted the diffraction patterns from 22° to 35°, where the most intensive peaks exist, and calculated the areal fractions for the peaks in this region (Supplementary Fig. 6a,b). When comparing the areal fractions from the original and new phases among the conditions, Bulk/PC has the lowest and Nano/DEGDME shows the highest intensities from the original phase, indicating that the degree of reversibility depends on cycling conditions. In parallel, as Bulk/PC showed the lowest and Nano/DEGDME showed the highest capacity

after the first cycle, we hypothesized that the reversible phase transformation on cycling is essential for effective sodium storage in Na$_2$C$_6$O$_6$ over multiple cycles.

To probe the phase transformation in more detail, in situ synchrotron XRD was performed under the Nano/DEGDME condition (Fig. 2a). As expected, we clearly observed the phase transformation from α to γ during the initial plateau at 2.0 V of discharge (~1.5 Na insertion), showing the gradual increase and decrease of the characteristic peaks from the γ-phase and the α-phase, respectively. After the disappearance of the α-phase, further discharge to 1.0 V (~0.5 Na insertion) resulted in the rise of a shoulder peak at q of 2.74, suggesting another phase transition. On charging from 1.0 V to 2.4 V (~1.0 Na extraction), we observed multiple steps of peak evolution in the q range of 2.7 to 2.8, in accordance with the multiple plateaus in the voltage profile; but the peaks from the original α-phase were

Fig. 2 | Phase transformation of Na$_2$C$_6$O$_6$ during sodiation/desodiation processes. a, In situ synchrotron XRD patterns of nanoparticle electrodes collected for every 0.1 Na-stoichiometry change, and the corresponding voltage profile of the Na$_2$C$_6$O$_6$ electrode in a pouch cell at 30 mA g^{-1}. The red and blue dotted lines correspond to Bragg peaks from γ-Na$_{2.5}$C$_6$O$_6$ and α-Na$_2$C$_6$O$_6$, respectively. **b**, Crystal structure change from γ-Na$_{2.5}$C$_6$O$_6$ to α-Na$_2$C$_6$O$_6$. We attribute the distinctive plateau around 3.0 V highlighted in a circle in **a** to this phase transformation.

not evolved yet. Then, when charging to 2.9 V, a positive shift in the characteristic peaks of the γ-phase was observed, which is in line with the results from DFT calculations (Supplementary Fig. 6c). On charging from 2.9 V to 3.2 V, we finally observe a two-phase region, corresponding to phase transformation from γ-$Na_{2.5}C_6O_6$ to α-$Na_2C_6O_6$ (Fig. 2b), demonstrating the reversible phase transition during the discharge/charge process. We attribute the distinctive plateau around 3.0 V in Nano/DEGDME (Fig. 2a, highlighted in a circle) to this two-phase region, which was not observed in the voltage profiles from other conditions (Fig. 1c). During the phase transition, the interlayer distance decreases, as the q of the (400) peak in α-$Na_2C_6O_6$ (2.16 Å^{-1}) is higher than the q of the (002) peak in γ-$Na_{2.5}C_6O_6$ (2.13 Å^{-1}). On the contrary, in Nano/PC, the phase transformation during cycling was not reversible, and the γ-phase formed during sodiation was still dominant when charged to 3.2 V (Supplementary Fig. 7b).

Overpotential for the γ- to α-phase transformation

We hypothesize that there is a large activation barrier, which varies with reaction conditions, causing a large overpotential for the γ- to α-phase transformation during desodiation. To assess this overpotential, we changed the charge cutoff voltages for cycling (Fig. 3). Originally, as overcharging can extract the original sodium ions holding the adjacent $C_6O_6^{2-}$ layers in the structure leading to dissolution of the $Na_2C_6O_6$ into the electrolyte[13], previous studies typically kept the charge cutoff below 3.2 V for stable cycling. Nevertheless, we overcharged the electrode to enable the kinetically hindered phase transition under conditions with limited electrochemical performances. In Nano/PC, after cycling in the stable potential range of 1.0 to 3.0 V (first to third, Supplementary Fig. 8a) followed by cycling with increased charge cutoff up to 3.3 V (Fig. 3b, fourth–fifth cycles), the electrode cycled with even higher charge cutoff up to 3.5 V (Fig. 3c, fifth–eighth cycles). We note that there was gradual evolution in discharge profiles, and eventually the pronounced plateau at 2.0 V reappeared in the last cycle (eighth cycle), similar to what was observed in DEGDME in the potential range of 1.0 to 3.2 V. The appearance of the original discharge plateau at 2.0 V after the first cycle indicates that it is also possible to restore α-$Na_2C_6O_6$ in PC with an increased overpotential; however, this exceeds the stable potential window of $Na_2C_6O_6$ (Supplementary Fig. 9). We further tested the $Na_2C_6O_6$ electrode in 1 M $NaPF_6$ in ethylene carbonate/diethyl carbonate (50:50, v/v) and tetraethylene glycol dimethyl ether (TEGDME) electrolytes with and without overcharging, and observed similar trends (Supplementary Fig. 10). Note that, in DEGDME, when the nanoparticle electrode is cycled below 2.9 V (Fig. 3d and Supplementary Fig. 8b), the voltage profile was similar to that observed in other conditions, showing a significant decrease in the reversible capacity after the first cycle while having a negligible capacity from the plateau at 2.0 V. Once charged to 3.2 V in the fourth cycle (Fig. 3e,f), the following discharge/charge profile became consistent with our result in Fig. 1c. Therefore, we concluded that the γ- to α-phase transformation during desodiation is feasible irrespective of the electrolytes but exhibits different overpotentials.

Changes in reaction kinetics after the first cycle
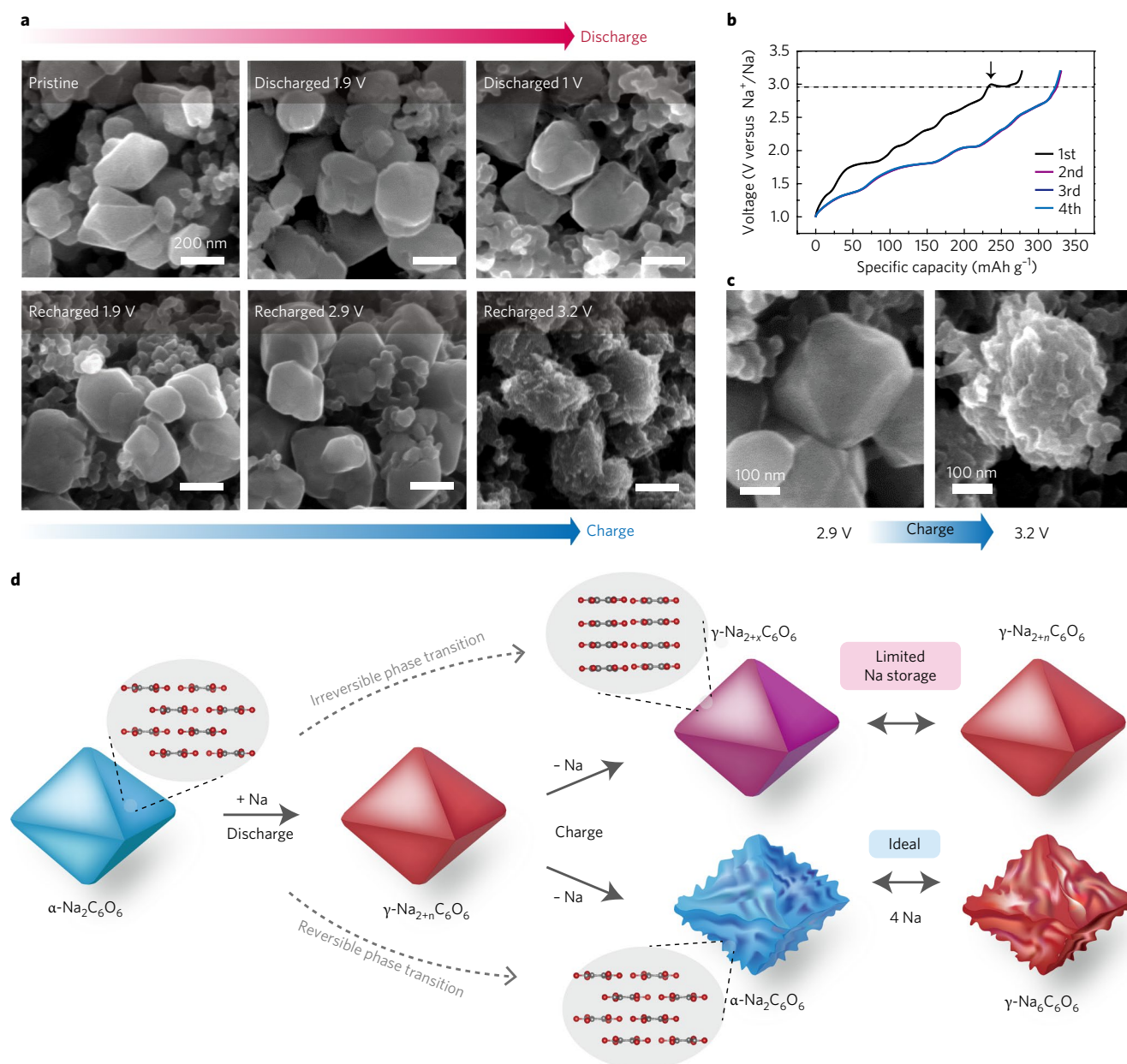
Interestingly, the distinctive plateau around 3.0 V with an overshoot that originated from the γ- to α-phase transformation in the first cycle no longer appears in following cycles in Nano/DEGDME (Fig. 4b). Moreover, in the second cycle, the diffraction peaks from the α-phase start to reappear even at 2.2 V (Supplementary Fig. 11), being much earlier than the first cycle. We hypothesized that this is indicative of faster kinetics for the γ- to α-phase transformation, and we were able to explain this by monitoring sodium-driven morphological changes during the first cycle by scanning electron microscopy. As shown in Fig. 4a, the pristine electrode consists of 300-nm-sized $Na_2C_6O_6$ particles and conductive carbon particles
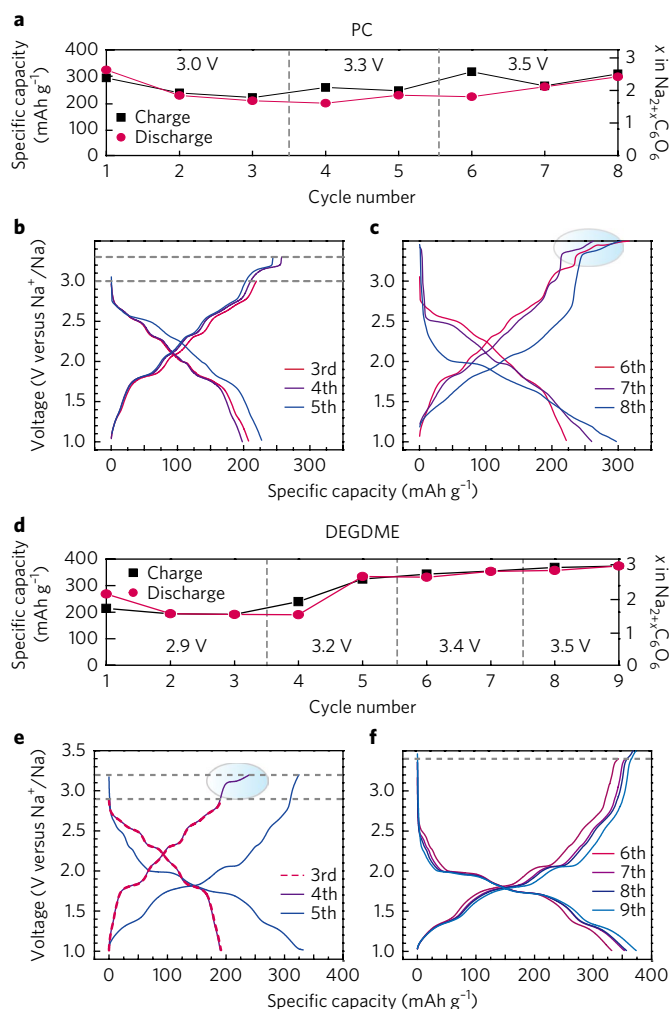
Fig. 3 | Voltage profile evolution of $Na_2C_6O_6$ during sodiation/desodiation processes. a–c, Evolution of discharge/charge curves of a $Na_2C_6O_6$ Nano electrode in PC during sequential changes of charge cutoff voltages from 3.0 V (1–3 cycles) to 3.3 V (4–5 cycles), and to 3.5 V (6–8 cycles). Specific capacity changes with charge cutoff voltage changes (**a**); voltage profiles of 3–5 cycles (**b**); and voltage profiles of 6–8 cycles (**c**). **d–f,** Evolution of discharge/charge curves of a $Na_2C_6O_6$ Nano electrode in DEGDME during sequential changes of charge cutoff voltages from 2.9 V (1–3 cycles), to 3.2 V (4–5 cycles), to 3.4 V (6–7 cycles), and to 3.5 V (8–9 cycles). Specific capacity changes with charge cutoff voltage changes (**d**); voltage profiles of 3–5 cycles (**e**); and voltage profiles of 6–9 cycles (**f**). The horizontal dashed lines indicate the charge cutoff voltage for each step. The plateau originating from the γ-$Na_{2.5}C_6O_6$ to α-$Na_2C_6O_6$ phase transition is highlighted in a circle.

that are smaller than 50 nm. On sodiation, the nanoparticles maintained the initial structure as a whole; when recharging 2.9 V, they still showed a similar morphology. In contrast, once charged up to 3.2 V, in which case the electrode fully recovered the original α-phase, we observed a noticeable change in the particle morphology. As shown in Fig. 4c with high magnification, nanosized grains smaller than 50 nm were formed within the particle, while maintaining the integrity of the network structure in the following cycles (Supplementary Fig. 12). On the other hand, we did not see any morphological evolution of nanoparticles in PC electrolyte (Supplementary Fig. 13), in line with our observation of cycled bulk electrodes (Supplementary Fig. 2).

We hypothesized that the large activation barrier for phase transformation resulted in metastable species γ-$Na_{2.5}C_6O_6$ during the first

Fig. 4 | Morphological changes during reversible phase transformation and proposed redox mechanism for sodium storage of Na$_2$C$_6$O$_6$. a, Ex situ SEM images of Nano electrodes at different states of charge during the first cycle in DEGDME (scale bar represents 200 nm). **b,** Charge profiles in Nano/DEGDME for four cycles. The distinctive plateau around 3.0 V with an overshoot (as indicated with an arrow) no longer appears in the following cycles. **c,** Magnified view of the dramatic morphology change of Na$_2$C$_6$O$_6$ nanoparticles during desodiation from 2.9 to 3.2 V. **d,** A schematic of the proposed de/sodiation mechanism of Na$_2$C$_6$O$_6$. During charging, the structural change from the α- to the γ-phase is kinetically suppressed. This leads to a premature desodiation, which results in limited sodium storage in subsequent cycles. Nevertheless, the reversible phase transformation becomes possible by decreasing the particle size and selecting a proper electrolyte, which in turn facilitates ideal four-sodium storage in Na$_2$C$_6$O$_6$.

charge process, because direct nucleation of α-Na$_2$C$_6$O$_6$ involving the entire slab shift may be kinetically very difficult. After downsizing the active particles, the kinetic barrier for reversible phase transformation would decrease. With electrochemical impedance spectroscopy, we confirmed a dramatic decrease in the apparent activation energy of Na$_{2.5}$C$_6$O$_6$ after nanostructuring (Supplementary Fig. 14). The lower activation energy indeed allowed direct nucleation of α-Na$_2$C$_6$O$_6$ below 2.2 V (Supplementary Fig. 11) and resulted in symmetric voltage profiles between discharge and charge in the second cycle (Fig. 1c, Nano/DEGDME).

To test the downsizing effect in PC electrolyte, nanoparticles of a few tens of nanometres (ex-Nano) were further prepared (Supplementary

Fig. 15). Note that the ex-Nano electrode exhibits no discharge profile hysteresis, and the redox activity no longer deteriorates after cycling, in contrast with the results from Bulk/PC and Nano/PC. Rather, the electrochemistry of ex-Nano in PC became similar to what was observed in DEGDME having spontaneous nanostructuring. This result further supports that the reversible γ- to α-phase transformation is feasible irrespective of the electrolytes, however the kinetic barrier for the transformation differs between the conditions.

Proposed mechanism
On the basis of the above investigation, we propose redox mechanisms for Na$_2$C$_6$O$_6$, as illustrated in Fig. 4d. During sodiation,
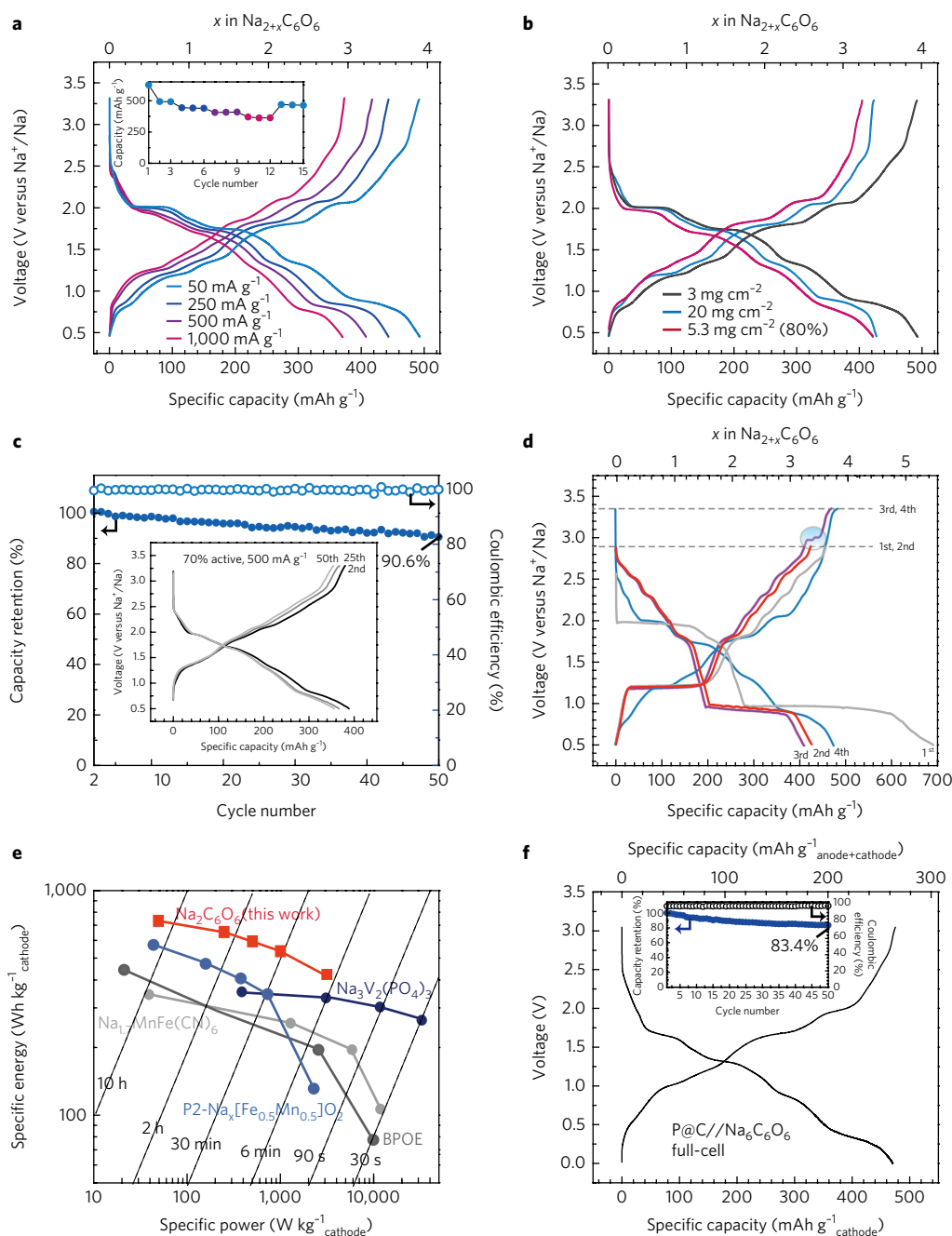
Fig. 5 | Electrochemical four-sodium storage of Na$_2$C$_6$O$_6$ electrodes in half-cells and full-cells. a, Rate capability and corresponding cycle performance (inset) of Na$_2$C$_6$O$_6$ electrodes from 0.5–3.3 V. **b**, Voltage profiles of Na$_2$C$_6$O$_6$ electrodes with high active content (80% Na$_2$C$_6$O$_6$, 5.3 mg cm^{-2}) and high mass loading (60% Na$_2$C$_6$O$_6$, 20 mg cm^{-2}) compared with the original condition (60% Na$_2$C$_6$O$_6$, 3 mg cm^{-2}). **c**, Cycle retention of Na$_2$C$_6$O$_6$ electrodes at 500 mA g^{-1} and the corresponding voltage profile (inset) for 50 cycles. **d**, Evolution of voltage profiles of Na$_2$C$_6$O$_6$ electrodes during sequential changes of charge cutoff voltages from 2.9 V (1–2 cycles) to 3.35 V (3–4 cycles). The horizontal dashed lines indicate the charge cutoff voltage for each cycle, and the circle indicates the plateau originating from the γ- to α-phase transition. **e**, Ragone plot of the Na$_2$C$_6$O$_6$ electrode compared with previously reported high-energy, high-power cathodes for Na cells. **f**, Voltage profile and capacity retention (inset) of a full-cell comprising of a Na$_6$C$_6$O$_6$ cathode and a phosphorous/carbon composite anode at 50 mA g^{-1}.

the α-phase of Na$_2$C$_6$O$_6$ is transformed into the γ-phase, which is energetically more favourable with the additional sodium. When removing the sodium during charging, the reverse structural change is kinetically suppressed, which leads to a premature desodiation in most cases at the voltage limit set to secure structural stability. Thus, the charged electrode remains in the γ-phase as partially sodiated species (Na$_{2+x}$C$_6$O$_6$), which significantly limits the redox capability of the electrode in subsequent cycles. Nevertheless, the reversible phase

transformation in the stable potential window becomes possible by decreasing the particle size and selecting a proper electrolyte. Among the electrolytes, DEGDME appears to be the most efficient in facilitating the phase transformation. According to the literature[20,21], when introducing DEGDME to sodium dianion salts, it is energetically preferable to form solvent-separated triple ions rather than contact triple ions, meaning that DEGDME molecules intervene between the cations and anions, and eliminate their contact. In contrast, other

solvents including TEGDME and carbonates instead result in contact ion multiples. Given the difference in ion association, we hypothesize that such strong solvation of DEGDME, dissociating Na^+ from the dianion salt, can facilitate sodium removal from the metastable γ-$Na_{2.5}C_6O_6$ during desodiation, which in turn lowers the kinetic barrier for the phase transformation. During sodiation/desodiation, the carbonyl groups in $Na_2C_6O_6$ are reduced and oxidized as redox centres as confirmed by reversible shifts to lower binding energy of carbon and oxygen atoms using X-ray photoelectron spectroscopy (for details, see Supplementary Fig 16 and Supplementary Note 2).

Four-sodium storage in $Na_2C_6O_6$

The understanding of the sodiation mechanism of $Na_2C_6O_6$ indeed allowed us to demonstrate a four-electron process in a Na-ion cell for the first time. This was demonstrated in an enlarged potential window from 0.5 to 3.2 V. As shown in Fig. 5a, a reversible capacity of 498 mAh g^{-1} was obtained at 50 mA g^{-1} in Nano/DEGDME after subtracting the capacity contribution from Super P (Supplementary Fig. 17), which is as high as 95% of the theoretical capacity. Even at the very high rates of 500 mA g^{-1} and 1000 mA g^{-1}, the electrode retained a specific capacity of 408 mAh g^{-1} and 371 mAh g^{-1}, respectively. With an increase of mass loading from 3 mg to 20 mg cm^{-2} (Fig. 5b), a capacity of 428 mAh g^{-1} was observed, which corresponds to an areal capacity of 8.56 Ah cm^{-2}. Also, with 80% active loading, $Na_2C_6O_6$ still showed a comparable profile with a capacity of 422 mAh g^{-1}. We hypothesize that the spontaneous nanostructuring in Nano/DEGDME enables $Na_2C_6O_6$ to facilitate efficient sodium storage in conditions that are known to be difficult for organic batteries, such as high mass loading (20 mg cm^{-2}), high active content (80%) and high current density (1 A g^{-1}). The $Na_2C_6O_6$ electrode showed good capacity retention on cycling (Fig. 5c). After 50 cycles, about 90.8% capacity of the second cycle was still available in the large potential window of 0.5 to 3.2 V at 500 mA g^{-1}. We note that more than 97% of the capacity was retained in the small potential window from 1.0 to 3.2 V for the three-electron redox reaction (Supplementary Fig. 18). We expect that further optimization in electrode microstructures would improve the cycle performance for the four-electron redox reaction by securing structural integrity of the electrode[22].

As shown in Fig. 5d, we observed the characteristic charge plateau around 3.0 V corresponding to phase transformation from γ-$Na_{2.5}C_6O_6$ to α-$Na_2C_6O_6$, and nanostructuring in parallel, in line with the voltage profiles obtained with the higher discharge cut-off at 1.0 V. In this enlarged potential window, the electrodes with bulk particles (Supplementary Fig. 19) or inappropriate electrolyte conditions (Supplementary Fig. 20) still exhibited limited reversible capacities, which validate our strategy to achieve complete sodium storage in $Na_2C_6O_6$.

In Nano/DEGDME, we obtained a maximum specific energy density of nearly 726 Wh kg^{-1}, where the weight is based on the cathode mass of $Na_2C_6O_6$, with a high energy efficiency above 87%, surpassing the performances of any other cathode candidates for SIBs. Note that the average operating voltage of $Na_2C_6O_6$ versus Na^+/Na is around 1.5 V, which is lower than that of transition-metal-based cathode candidates for SIBs. Nevertheless, we claim that the strong advantage of using renewable resources from biomass while exhibiting an energy density as high as 726 Wh kg^{-1} provides rationale for using this compound as a cathode for grid-scale applications. The Ragone plot (Fig. 5e) shows that the $Na_2C_6O_6$ electrode outperforms the reported high-performance NIB electrodes[23–26]. Our $Na_2C_6O_6$ electrode showed remarkable energy density throughout a wide range of rates, delivering a specific energy of 410 Wh kg^{-1} within 7.8 min corresponding a specific power of 3151 W kg^{-1}.

Full-cell performance

Finally, we built full-cells with $Na_2C_6O_6$ by coupling it with other Earth-abundant anodes. We first selected phosphorous encapsulated

in a carbon scaffold (P@C) as an anode, which provides the highest specific capacity among the anode materials for SIBs reported so far[27,28]. As shown in Supplementary Fig. 21, the P@C anode exhibits a reversible capacity of 1,725 mAh g^{-1} versus sodium (theoretical capacity 2,595 mAh g^{-1}). The full-cell was assembled with a pre-cycled P@C anode for high coulombic efficiency and an electrochemically sodiated $Na_6C_6O_6$ cathode. The full-cell exhibits a reversible capacity of 265 mAh g^{-1} at 50 mA g^{-1} based on the total mass of cathode and anode, resulting in an remarkable energy density as high as 281 Wh kg^{-1} (Fig. 5f), which is the highest value based on the total mass of cathode and anode among any reported sodium full-cells (Supplementary Table 1)[29–33]. We also demonstrated an all-organic sodium full-cell with an organic salt anode, disodium terephthalate ($Na_2C_8H_4O_4$)[34,35], exhibiting a full-cell energy density of 141 Wh kg^{-1} (Supplementary Fig. 22), which is an example of a sustainable battery that comprises only carbon, oxygen and sodium atoms. We expect that further optimization of mass balance between cathode and anode would improve the energy density and cycle performance of full-cells.

Conclusions

We achieved full utilization of four-Na-ion storage in $Na_2C_6O_6$ based on the understanding of the redox mechanism associated with structural and morphological changes during cycling. We discovered that the deteriorating redox activity of $Na_2C_6O_6$ on cycling originated from an irreversible phase transformation, and identified active-particle sizes and electrolyte conditions as key factors to complete the phase transformation during desodiation. Unexpectedly, spontaneous formation of nanostructures during the first γ- to α-phase transformation enabled facile phase transformation in the following cycles, which provided a mechanism not only for enabling four-sodium storage but also for realizing high-rate capability of electrode materials. The resulting electrochemical performances of the $Na_2C_6O_6$ electrode including a specific energy density of 726 Wh $kg^{-1}_{cathode}$, a high energy efficiency of above 87%, and a good cycle retention surpass any reported performances of cathode candidates for SIBs. This work presents new insights into complete utilization of electrochemical performances of active compounds, which will provide cheaper and greener ways to store renewable energy.

Methods

Sample preparation. Pristine $Na_2C_6O_6$ powder was used as the bulk particle sample as received (Sigma-Aldrich). To obtain $Na_2C_6O_6$ micro- and nanoparticles, we used an antisolvent precipitation process leveraging the poor solubility of $Na_2C_6O_6$ in organic solvents. For $Na_2C_6O_6$ nanoparticles, the pristine $Na_2C_6O_6$ was dissolved in water at 80 °C (4 mg ml^{-1}) and mixed with ethanol in a ratio of 1:10 in volume. For $Na_2C_6O_6$ microparticles, we used 0.4 mg ml^{-1} $Na_2C_6O_6$ aqueous solution. After sonication at room temperature for 5 min, precipitates were collected by vacuum filtration and dried in a vacuum oven at 70 °C for 1 h. To prepare $Na_2C_6O_6$ particles of a few tens of nanometres (ex-Nano), we incubated $K_2C_6O_6$ (Sigma-Aldrich) in a saturated solution of $NaPF_6$ in dimethoxyethane (DME) for one day at room temperature. To prepare electrodes, $Na_2C_6O_6$ particles were mixed with carbon-black conductive additive (Super P, TIMCAL) and polytetrafluoroethylene (PTFE) binder (Sigma-Aldrich). A 6:3:1 weight ratio was used to prepare typical electrode samples and 7:2:1 or 8:1:1 weight ratios were used to obtain high-active-content electrode samples. The dry mixtures were ground in an agate mortar with a few drops of ethanol and rolled into a free-standing film on a glass surface. After drying in a vacuum oven at 70 °C for 1 h, the samples were cut into 1 cm^2 circular discs with a mass loading of 2–3 mg for typical electrodes and 20 mg for a high-mass-loading sample.

Electrochemical measurements. In an Ar-filled glovebox, the $Na_2C_6O_6$ electrode was assembled into a 2032 type coin cell with a polymer separator (Celgard 2250) and Na metal (Sigma-Aldrich). Sixty microlitres of an electrolyte solution was added to the separator. $NaClO_4$ (1.0 M) in PC, $NaPF_6$ (1.0 M) in EC/DEC, $NaPF_6$ (0.6 M) in DEGDME and $NaPF_6$ (0.6 M) in TEGDME were used as electrolytes. The resulting coin cells were loaded into a battery tester (Arbin Instruments). Cyclic voltammetry and electrochemical impedance spectroscopy were performed with the coin cells using a VSP potentiostat (Biologic). Electrochemical impedance spectroscopy was performed with a 10 mV amplitude between 200 mHz and 1 MHz. Sodium-ion full-cells were constructed using electrochemically sodiated $Na_6C_6O_6$ electrodes. Both disodium terephthalate ($Na_2C_8H_4O_4$) and phosphorous/

carbon composite were used as the anodes to build the all-organic sodium full-cell and the high-energy full-cell, respectively. The $Na_2C_8H_4O_4$, anode was prepared by mixing 60 wt% active materials with Super P (30 wt%) and PTFE (10 wt%). The P@C anode comprised 40% of phosphorous encapsulated in porous carbon with 10 wt% PVDF. Before the full-cell assembly, the anode was pre-cycled once versus sodium to reach a high coulombic efficiency. The mass ratio between the cathode and the anode was about 3.8:1 for the $P@C//Na_6C_6O_6$ full-cell and 0.7:1 for the $Na_2C_8H_4O_4//Na_6C_6O_6$, full-cell, so that the cell capacity was determined by the cathode with 20% excess of anode capacity. Charge and discharge measurements were carried out between 0 and 3.1 V at 50 mA g^{-1}.

Characterization. For ex situ scanning electron microscopy (SEM) and XRD characterizations of working electrodes, coin cells were cycled to a certain state of charge and disassembled in an Ar-filled glovebox. To protect the electrode from ambient air during the XRD measurement, the electrodes were covered with Kapton tape on glass slides. We noticed that the new phase in the cycled electrode was observable only with proper air-tight sealing during XRD measurements (Supplementary Fig. 23). The XRD pattern was measured with a PANalytical X'Pert PRO X-ray diffractometer with Cu Kα radiation. SEM observation was performed with an FEI XL30 Sirion SEM at 5.0 kV without any metal coating. In situ synchrotron XRD was conducted in transmission mode using an incident beam energy of 15.5 keV at beamline 1–5 of the Stanford Synchrotron Radiation Lightsource at the SLAC National Accelerator Laboratory. XRD patterns were collected using an acquisition time of 15 s per spectrum from an Al-coated pouch-type battery cell pressurized by beryllium windows during galvanostatic discharge and charge at 30 mA g^{-1} with SP-150 (Biologic), which exhibits similar electrochemical performances to a coin cell (Supplementary Fig. 24). Contact angle measurements were recorded using a First Ten Angstroms FTA200 equipped with a CCD (charge-coupled device) camera.

References

1. Dunn, B., Kamath, H. & Tarascon, J.-M. Electrical energy storage for the grid: a battery of choices. *Science* **334**, 928–935 (2011).
2. Choi, J. W. & Aurbach, D. Promise and reality of post-lithium-ion batteries with high energy densities. *Nat. Rev. Mater.* **1**, 16013 (2016).
3. Kim, H. et al. Recent progress in electrode materials for sodium-ion batteries. *Adv. Energy Mater.* **6**, 1600943 (2016).
4. Kundu, D., Talaie, E., Duffort, V. & Nazar, L. F. The emerging chemistry of sodium ion batteries for electrochemical energy storage. *Angew. Chem. Int. Edn* **54**, 3431–3448 (2015).
5. Larcher, D. & Tarascon, J. M. Towards greener and more sustainable batteries for electrical energy storage. *Nat. Chem.* **7**, 19–29 (2015).
6. Muench, S. et al. Polymer-based organic batteries. *Chem. Rev.* **116**, 9438–9484 (2016).
7. Häupler, B., Wild, A. & Schubert, U. S. Carbonyls: powerful organic materials for secondary batteries. *Adv. Energy Mater.* **5**, 1402034 (2015).
8. Song, Z. & Zhou, H. Towards sustainable and versatile energy storage devices: an overview of organic electrode materials. *Energy Environ. Sci.* **6**, 2280–2301 (2013).
9. Zhao, Q. et al. Oxocarbon salts for fast rechargeable batteries. *Angew. Chem. Int. Edn* **55**, 12528–12532 (2016).
10. Chen, H. et al. From biomass to a renewable $Li_xC_6O_6$ organic electrode for sustainable Li-ion batteries. *ChemSusChem* **1**, 348–355 (2008).
11. Chen, H. et al. Lithium salt of tetrahydroxybenzoquinone: toward the development of a sustainable Li-ion battery. *J. Am. Chem. Soc.* **131**, 8984–8988 (2009).
12. Kim, H. et al. The reaction mechanism and capacity degradation model in lithium insertion organic cathodes, $Li_2C_6O_6$, using combined experimental and first principle studies. *J. Phys. Chem. Lett.* **5**, 3086–3092 (2014).
13. Chihara, K., Chujo, N., Kitajou, A. & Okada, S. Cathode properties of $Na_2C_6O_6$ for sodium-ion batteries. *Electrochim. Acta* **110**, 240–246 (2013).
14. Wang, C. et al. Manipulation of disodium rhodizonate: factors for fast-charge and fast-discharge sodium-ion batteries with long-term cyclability. *Adv. Funct. Mater.* **26**, 1777–1786 (2016).
15. Wang, Y. et al. Understanding the size-dependent sodium storage properties of $Na_2C_6O_6$-based organic electrodes for sodium-ion batteries. *Nano Lett.* **16**, 3329–3334 (2016).
16. Dinnebier, R. E., Nuss, H. & Jansen, M. Disodium rhodizonate: a powder diffraction study. *Acta Crystallogr., Sect. E* **61**, m2148–m2150 (2005).
17. Luo, C. et al. Self-assembled organic nanowires for high power density lithium ion batteries. *Nano Lett.* **14**, 1596–1602 (2014).
18. Yamashita, T., Momida, H. & Oguchi, T. First-principles investigation of a phase transition in $Na_xC_6O_6$ as an organic cathode material for Na-ion batteries: role of intermolecule bonding of C_6O_6. *J. Phys. Soc. Jpn* **84**, 074703 (2015).
19. Yamashita, T., Momida, H. & Oguchi, T. Crystal structure predictions of $Na_xC_6O_6$ for sodium-ion batteries: first-principles calculations with an evolutionary algorithm. *Electrochim. Acta* **195**, 1–8 (2016).
20. Bock, H., Naether, C. & Havlas, Z. Competing Na$^+$ solvation: ether-shared and ether-separated triple ions of perylene dianion. *J. Am. Chem. Soc.* **117**, 3869–3870 (1995).
21. Bock, H., Näther, C., Havlas, Z., John, A. & Arad, C. Ether-solvated sodium ions in salts containing π-hydrocarbon anions: crystallization, structures, and semiempirical solvation energies. *Angew. Chem. Int. Ed. Engl.* **33**, 875–878 (1994).
22. Li, Y. et al. Growth of conformal graphene cages on micrometre-sized silicon particles as stable battery anodes. *Nat. Energy* **1**, 15029 (2016).
23. Rui, X., Sun, W., Wu, C., Yu, Y. & Yan, Q. An advanced sodium-ion battery composed of carbon coated $Na_3V_2(PO_4)_3$ in a porous graphene network. *Adv. Mater.* **27**, 6670–6676 (2015).
24. Sakaushi, K. et al. Aromatic porous-honeycomb electrodes for a sodium-organic energy storage device. *Nat. Commun.* **4**, 1485 (2013).
25. Wang, L. et al. A superior low-cost cathode for a Na-ion battery. *Angew. Chem. Int. Edn* **52**, 1964–1967 (2013).
26. Yabuuchi, N. et al. P2-type $Na_x[Fe_{1/2}Mn_{1/2}]O_2$ made from earth-abundant elements for rechargeable Na batteries. *Nat. Mater.* **11**, 512–517 (2012).
27. Ramireddy, T. et al. Phosphorus-carbon nanocomposite anodes for lithium-ion and sodium-ion batteries. *J. Mater. Chem. A* **3**, 5572–5584 (2015).
28. Li, W. et al. Amorphous red phosphorus embedded in highly ordered mesoporous carbon with superior lithium and sodium storage capacity. *Nano Lett.* **16**, 1546–1553 (2016).
29. Guo, S. et al. A high-voltage and ultralong-life sodium full cell for stationary energy storage. *Angew. Chem. Int. Edn* **54**, 11701–11705 (2015).
30. Wang, S. et al. All organic sodium-ion batteries with $Na_4C_8H_2O_6$. *Angew. Chem. Int. Edn* **53**, 5892–5896 (2014).
31. Li, H. et al. An advanced high-energy sodium ion full battery based on nanostructured $Na_2Ti_3O_7/VOPO_4$ layered materials. *Energy Environ. Sci.* **9**, 3399–3405 (2016).
32. Xie, X. et al. Sn@CNT nanopillars grown perpendicularly on carbon paper: a novel free-standing anode for sodium ion batteries. *Nano Energy* **13**, 208–217 (2015).
33. Wang, Y., Xiao, R., Hu, Y.-S., Avdeev, M. & Chen, L. P2-$Na_{0.6}[Cr_{0.6}Ti_{0.4}]O_2$ cation-disordered electrode for high-rate symmetric rechargeable sodium-ion batteries. *Nat. Commun.* **6**, 6954 (2015).
34. Zhao, L. et al. Disodium terephthalate ($Na_2C_8H_4O_4$) as high performance anode material for low-cost room-temperature sodium-ion battery. *Adv. Energy Mater.* **2**, 962–965 (2012).
35. Park, Y. et al. Sodium terephthalate as an organic anode material for sodium ion batteries. *Adv. Mater.* **24**, 3562–3567 (2012).

Author contributions

M.L. carried out materials fabrication, characterization and testing. J.H. and M.L. performed in situ synchrotron XRD. K.L., J.H., M.F.T. and W.C.C. designed and constructed settings for in situ synchrotron XRD. Y.S. prepared the phosphorous/carbon composite. J.L. and D.F. provided constructive advice for experiments. M.L. wrote the first draft. Z.B. and Y.C. revised the manuscript. All authors discussed the results and contributed to preparing the manuscript.

Competing interests

The authors declare no competing financial interests.

Additional information